Computing Rebar Layouts Aligned with the Principal Stress Directions: A Distance-Constrained Tracing Approach

2 authors:

Rafael Pastrana
Princeton University
11 PUBLICATIONS **88** CITATIONS

SEE PROFILE
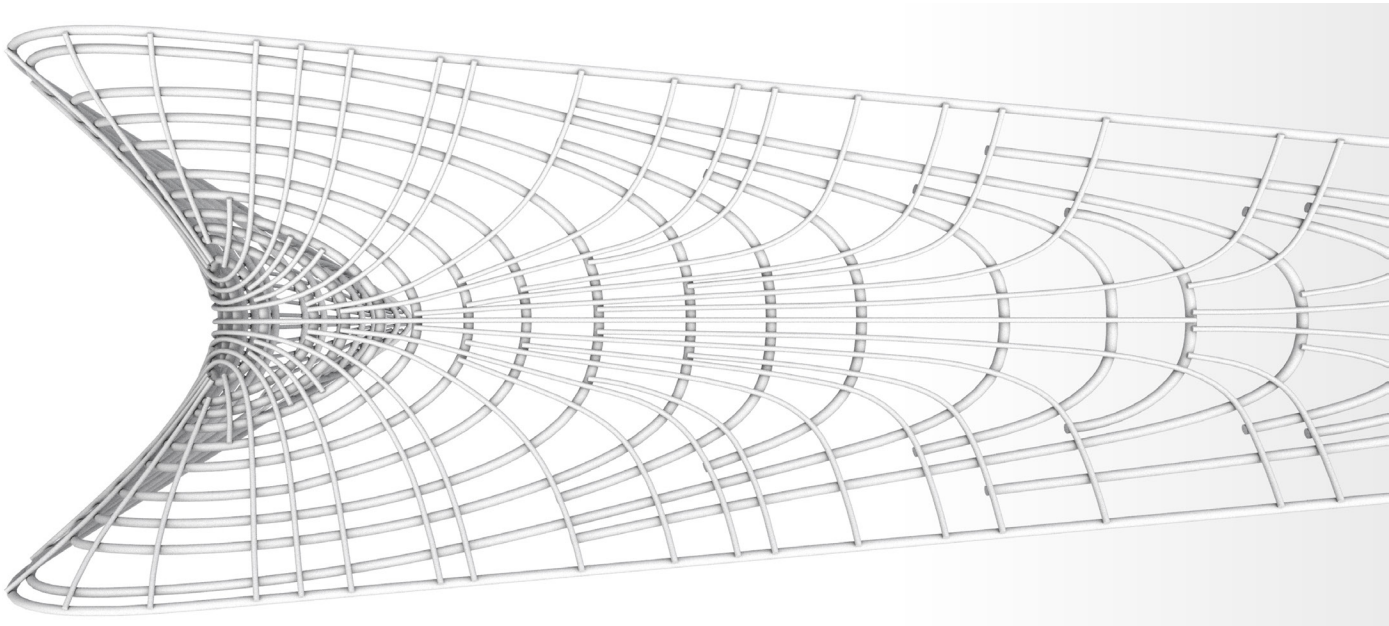
Zhao Ma
ETH Zurich
8 PUBLICATIONS **88** CITATIONS

SEE PROFILE

**LEAVE THIS PAGE BLANK
DO NOT DELETE THIS PAGE**

Computing Rebar Layouts Aligned with the Principal Stress Directions

A Distance-Constrained Tracing Approach

Rafael Pastrana
Princeton University

Zhao Ma
ETH Zurich

1

ABSTRACT

Reducing the consumption of carbon-intensive materials such as rebar steel is crucial to mitigate the environmental impact associated with architectural surfaces built with reinforced concrete. While digital fabrication and modern structural analysis tools offer opportunities to decrease rebar consumption, new computational approaches to create material-minimizing rebar layouts are required to effectively harness such potential.

This paper presents a computational method to generate rebar layouts aligned with the principal stress directions on architectural surfaces. This method combines a reinforced concrete design module based on current structural engineering codes, and a distance-constrained algorithm with adaptive seeding that iteratively traces evenly spaced rebars that follow a structurally optimal force flow. After its application to a flat slab and a folded shell, we demonstrate that the principal stress-aligned rebar layouts require up to 32% less steel than a single orthogonal rebar grid to resist an applied load.

Our work highlights the potential of integrating design computation and structural engineering to advance research in the field of digital reinforcement, and to foster environmentally-aware design practices.

1   Render of a rebar layout aligned with the principal stress directions on a folded shell.

INTRODUCTION

Reinforced Concrete

Ranging from flat slabs to free-form shells, the breadth of architectural surfaces built with reinforced concrete (RC) highlights the relevance of RC as one of the most prominent materials in the building industry (Figures 2.1 and 2.2). The inherent strength of RC, achieved by combining the compressive properties of concrete with the tensile capabilities of reinforcement steel, enables the design of durable structures capable of spanning long distances and supporting significant external loads (Addis 2015).

However, RC is also one of the most carbon-intensive materials in the construction sector, and its use aggravates current environmental concerns. The production of cement, a key component of concrete, is responsible for approximately 7% of the global greenhouse gas emissions (Andrew 2019). The extraction, processing, and transportation of other raw materials involved in the production of concrete inflate its carbon footprint.

Fostered by advancements in computation, structural optimization, and digital fabrication, the rising field of digital concrete opens up possibilities to design material-efficient structures by depositing concrete only where it is structurally necessary (Wangler et al. 2019). By employing technologies such as additive manufacturing, innovative designs have been materialized, including 3D-printed columns (Lloret et al. 2015; Anton et al. 2020), trusses (Lowke et al. 2021), slabs (Jipa et al. 2019; Oval et al. 2023), and bridges (Bhooshan et al. 2022), showcasing the potential of digital concrete to foster sustainability.

Digital Reinforcement

Although minimizing concrete consumption is crucial, diminishing the amount of rebar steel in RC structures is also necessary. The production of steel for construction contributes to nearly half of the greenhouse gas emissions of RC (Wang et al. 2007). In architectural surfaces built with RC, like flat slabs, rebar accounts for up to 60% of the embodied carbon (Miller et al. 2015). Therefore, the growing progress of digital concrete should be complemented with advancements in digital reinforcement research (Asprone et al. 2018) to holistically curb the negative impact that RC surfaces have on the environment.

Promising efforts are underway in this direction. These include the application of winded carbon fiber reinforcement in slabs (Oval et al. 2020) and rebar cages that dispense formwork for doubly curved surfaces (Hack and Lauer 2014; Mirjan et al. 2022). We note that the latter example still adheres to arranging rebar in a single
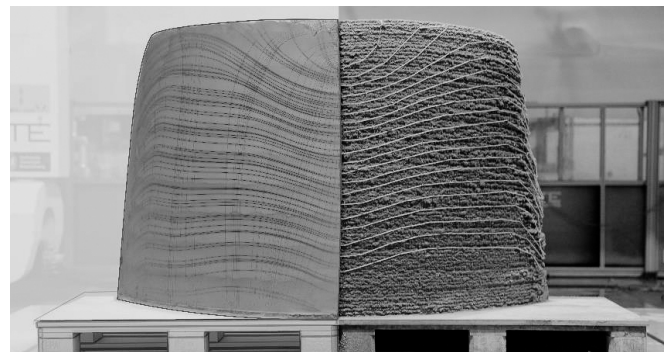
2.1

2.2

3.1

3.2

4.1

4.2

orthogonal grid, akin to conventional on-site practices, instead of fully leveraging the capabilities of robotic arms to deposit materials along arbitrary directions with high precision (Figure 3.1). In contrast, recent studies (Ma et al. 2020; Gantner et al. 2022) have demonstrated the materialization of reinforcement layouts that follow the flow of forces through digital fabrication techniques (Figure 3.2).
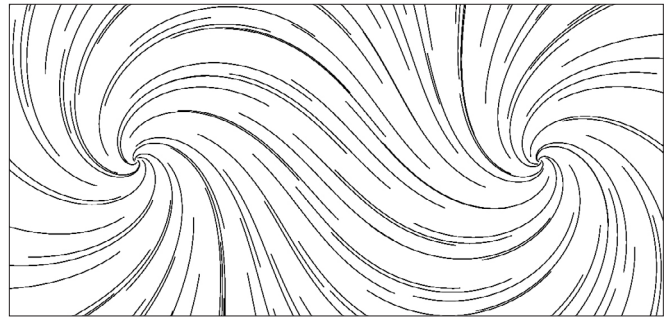
Principal Stress Directions

The principal stress directions (PSDs) encode an optimal flow of forces in a structure. These directions represent the local orthonormal basis of a state of plane stress where axial stresses are maximized and shear stresses vanish (Hibbeler 2017). Notable architectural works by Hecker and Nervi (Hecker and Hecker 2009; Nervi et al. 2010) exemplify the benefits of aligning load-bearing material with the PSDs at the architectural scale, as the alignment reduces the amount of material required to resist loads (Pellis and Pottmann 2018; Ma et al. 2020).
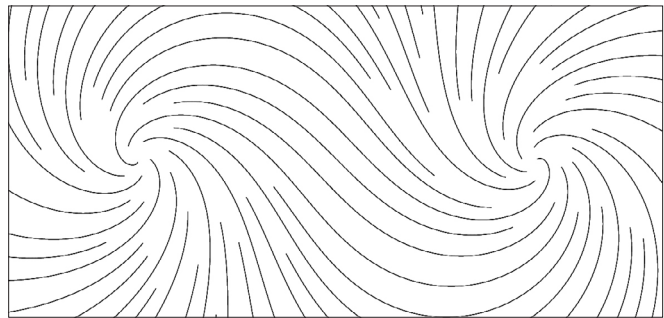
The integration of PSDs creates a network of curves, known as the principal stress lines, which can be used as the geometry of a material-minimizing rebar layout. Such integration can be done analytically (Michell 1904) or numerically with modern structural analysis tools (Michalatos and Kaijima 2014; Preisinger and Heimrath 2014). However, the majority of such analysis tools are designed for visualizing stress flow, and not for generating rebar layouts that comply with distance or fabrication constraints, due to the presence of undesired geometric discontinuities, bundles, and intersections. Tam and Mueller (2015) proposed a rule-based algorithm to address these geometric issues, but the efficacy of their approach, like other current methods, depends on the manual selection of appropriate seed points (Figures 4.1 and 4.2).

Contributions

Digital fabrication technologies and structural analysis tools enable the construction and mechanical assessment of bespoke rebar configurations. However, it is necessary to develop computational methods that support the design of material-minimizing rebar layouts to effectively diminish rebar consumption in the field and the associated emissions produced by RC surfaces.

In this paper, we introduce a computational method that automates the generation of rebar layouts aligned with the PSDs (Figure 1). This method supports the exploration of the geometry of such layouts during the conceptual design stage for different loading and support conditions, as well as for distinct rebar diameters and tracing parameters. Our method combines an RC design module based on current structural engineering codes with a distance-constrained tracing algorithm to generate material-minimizing layouts. This algorithm iteratively traces rebar following the optimal flow of forces on a manifold mesh, while it automatically adjusts the placement of seed points to achieve an evenly spaced distribution of rebars graded according to the tensile stresses acting on an RC surface.

DESIGN METHOD

Figure 5 provides an overview of the three parts that compose our method. Besides the numerical parameters, the input is a mesh representing the surface to be designed, and the output is the geometry of a rebar layout, generated as one set of polylines per PSD. We implement this method using COMPAS, a framework for computational research in architecture and structures (Van Mele et al. 2017), and Karamba3D (Preisinger and Heimrath 2014).
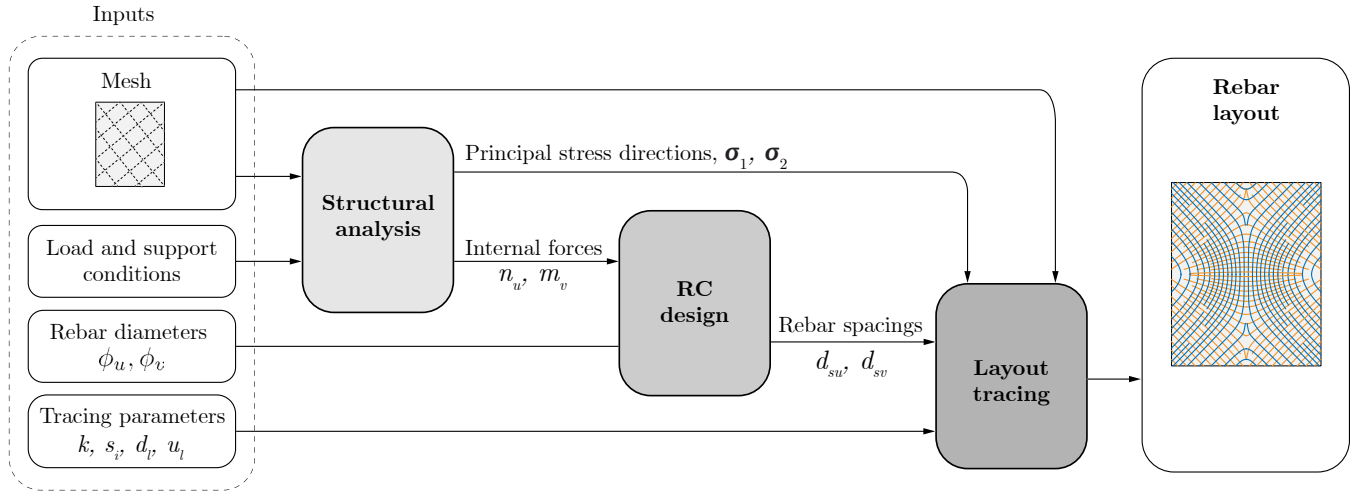
5　Overview of the method to compute rebar layouts aligned with the PSDs.

Structural Analysis

We conduct a linear elastic structural analysis to obtain the internal forces in an RC surface, given specific load and support conditions.

The analysis takes as input an orientable, manifold mesh with sufficient density to accurately capture the mechanical behavior of the structure. We then apply the material properties, cross-sections, support conditions, and loads to the mesh. We also define two orthogonal vectors $\mathbf{u}$ and $\mathbf{v}$ per mesh face that set the reference axes along which the analysis results are expressed. In our analyses, all the structural information is output at the centroids of the mesh faces.

Figure 6 illustrates the configuration of the calculated internal forces, which includes the magnitude of the three axial forces (n_{uu}, n_{vv}, n_{uv}) and the three bending moments (m_{uu}, m_{vv}, m_{uv}). We also estimate the pair of PSDs at three locations along the thickness of the structure: the top (σ_1^t, σ_2^t), the middle (σ_1^c, σ_2^c), and the bottom (σ_1^b, σ_2^b) layers. We select the PSDs with the highest tensile force among the three layers at each mesh face and use these to trace a rebar layout. We denote these direction vectors as σ_1 and σ_2 in the following. The locations where we extract the internal forces and the PSDs are in line with the sandwich model we use for RC design.

Reinforced Concrete Design

We implement a modified version of the three-layer sandwich model (Lourenço and Figueiras 1995; Blaauwendraad 2010) to estimate the area of rebar steel and the spacing between rebars that the RC surface requires to withstand tensile stresses.

The mathematical formulation of the sandwich model is compact and accounts for the combined action of membrane forces and bending moments. Moreover, it is included in current engineering codes (ECS 2005; IFSC 2008), making it compatible with practical design applications. In the sandwich model, every mesh face on the surface is split into a top, a middle core, and a bottom layer. The top and bottom layers are separated by a distance h measured between the midpoints of each layer (Figure 7).

The sandwich model outputs the cross-section area or reinforcement per width unit, a_{su} and a_{sv}, at the top and bottom layers of the mesh faces. The model inputs are the surface thickness t, the steel yield stress f_y and the rebar diameter ϕ_u and ϕ_v along axes $\mathbf{u}$ and $\mathbf{v}$, respectively. We assume adequate bonding between concrete and rebar, and that the thickness of the RC surface is sufficient to resist shear forces without rebar stirrups.

Conventional applications of the sandwich model result in two rebar layouts, one hosted in the top layer and another in the bottom layer. We generate a single rebar layout instead because the out-of-plane bending moments m_{uu}, m_{vv} and m_{uv} exert tensile stresses only on one side of the surface, either at the top or at the bottom. As we target the design of material-efficient structures, it would be redundant to add two layers of rebar if only one suffices. Hence, we shift the geometry of the layout to the top or to the bottom layer based on the acting tensile stresses (Figure 8).

The tension forces for rebar design in the top and bottom layers n_{su}^t, n_{sv}^t, n_{su}^b and n_{sv}^b only include the contribution of the bending moments (Equations 1 and 2). The effect of the in-plane axial forces are accounted for in Equation 3:
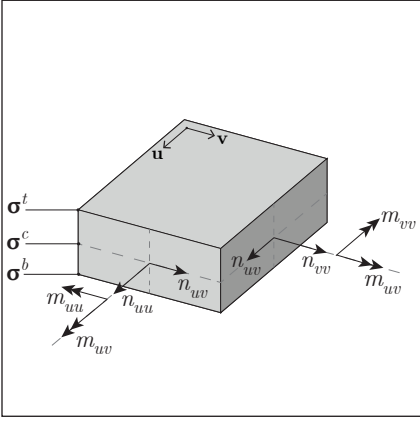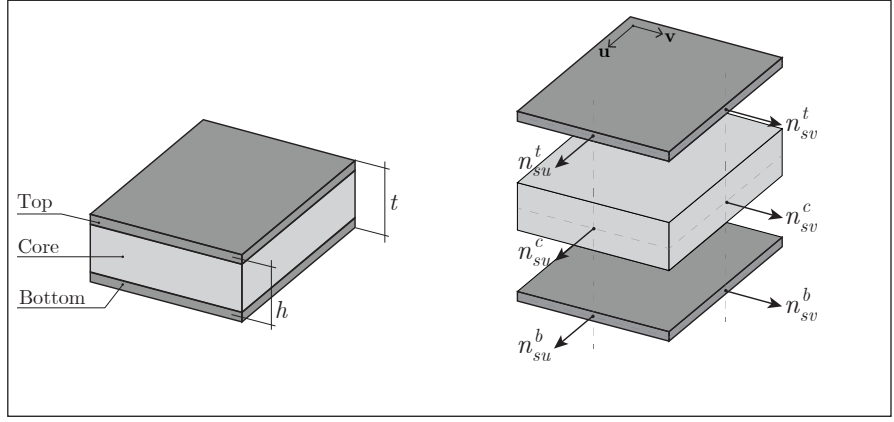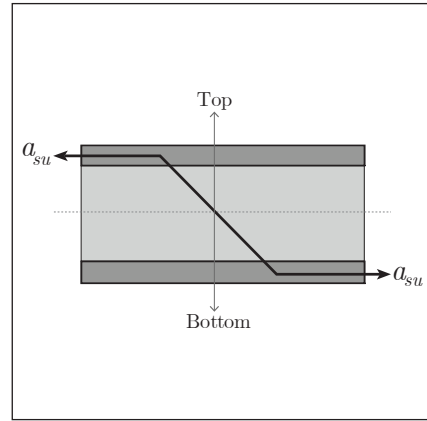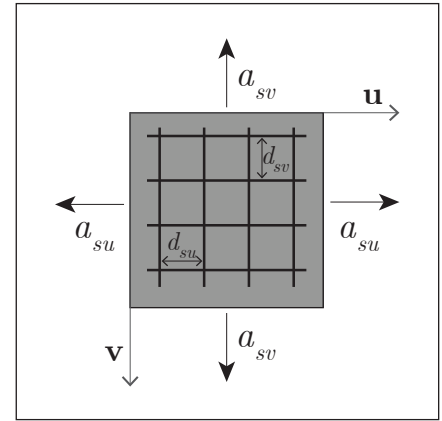
6   Internal forces in an RC surface.

7   Sandwich model for RC design.

8   Rebar area shift between sandwich layers.

9   Rebar area distribution per sandwich layer.

$$n_{su}^t = \frac{m_{uu}}{h} + \frac{m_{uv}}{h} \qquad n_{sv}^t = \frac{m_{vv}}{h} + \frac{m_{uv}}{h} \tag{1}$$

$$n_{su}^b = -\frac{m_{uu}}{h} - \frac{m_{uv}}{h} \qquad n_{sv}^b = -\frac{m_{vv}}{h} - \frac{m_{uv}}{h} \tag{2}$$

$$n_{su}^c = n_{uu} + \frac{n_{uv}}{2} \qquad n_{sv}^c = n_{vv} + \frac{n_{uv}}{2} \tag{3}$$

As negative values are expected from calculating the tensile forces on the layers, denoting no need for reinforcement (Blaauwendraad 2010), the terms n_{su}^c, and n_{sv}^c are added only to the maximum values of n_{su}^t, n_{sv}^t, n_{su}^b, and n_{sv}^b. We discard eccentricity effects. The calculated tensile forces are then condensed into n_{suu} and n_{svv} which represent the total tensile forces along the **u** and **v** reference directions:

$$n_{suu} = \max(n_{su}^t, n_{su}^b) + n_{su}^c$$
$$n_{svv} = \max(n_{sv}^t, n_{sv}^b) + n_{sv}^c \tag{4}$$

In Equation 5, we compute the cross-sectional area of rebar per unit width in the sandwich layers a_{su} and a_{sv} shown in Figure 9 based on the total tensile forces:

$$a_{su} = \frac{n_{suu}}{f_y} \qquad a_{sv} = \frac{n_{svv}}{f_y} \tag{5}$$

We then calculate the separation distances per reference direction, d_{su} and d_{sv}, with the input diameters ϕ_u and ϕ_v:

$$d_{su} = \frac{\pi \phi_u^2}{4\,a_{su}} \qquad d_{sv} = \frac{\pi \phi_v^2}{4\,a_{sv}} \tag{6}$$

The distances obtained with Equation 6 are stored in vectors $\boldsymbol{d}_{su}$ and $\boldsymbol{d}_{sv}$ with pointers to their corresponding location on the mesh to simplify their query during tracing. These distances modulate the separation between the rebars generated by the distance-constrained rebar tracing algorithm we develop in the following subsection.

By changing the diameters $\boldsymbol{\phi}_u$ and $\boldsymbol{\phi}_v$ we can tune the geometry of a rebar layout. Additionally, our method allows the definition of an individual diameter per mesh face to enable finer-grained control of the layout density. We illustrate the effect of choosing different global rebar diameters with two examples in the structural applications section.
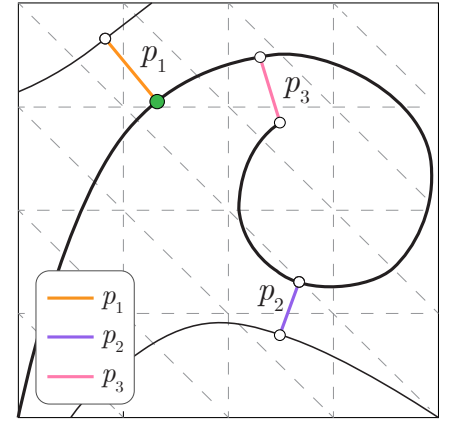
Rebar Layout Generation

We develop an algorithm to trace evenly-spaced rebars along the PSDs, building on the work of Jobard and Lefer (1997), Mebarki et al. (2005), and Tam and Mueller (2015). This algorithm iteratively integrates polylines on the mesh

Computing Rebar Layouts Aligned with the PSDs Pastrana and Ma
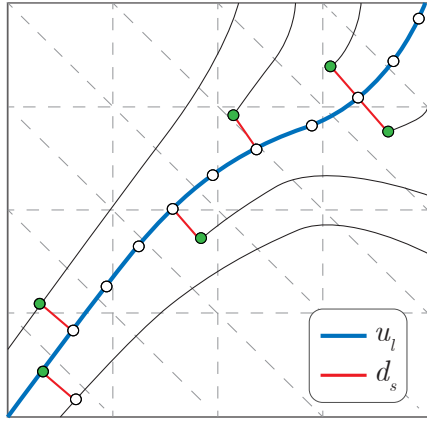
10.1
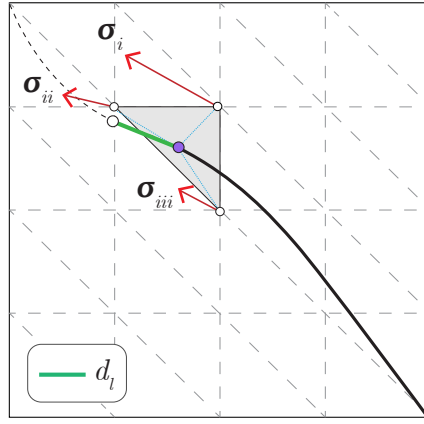
10.2

10.3

10 Rebar layout generation steps:

    10.1 Seed sampling on rebar polyline

    10.2 Direction interpolation, $k = 3$

    10.3 Distance control with proximity thresholds

representation of the input surface via bi-directional projective tracing. One polyline corresponds to the center-line of one rebar. To avoid rebar cluttering, and to minimize rebar consumption by placing material only where needed, the algorithm maintains the distance between rebars computed with Equation 6, while it traces rebar polylines.

The algorithm traces one polyline at a time until a priority queue is empty, or until the generation of more rebars is unfeasible due to distance, seeding or geometric constraints. We run the algorithm twice to generate a rebar layout, once per set of PSDs, σ_1 and σ_2. The four operations involved in the generation of a rebar layout are:

- Automating the selection of good initial seeds.
- Constructing a priority queue to ensure adequate densi-fication of the rebar layout.
- Calculating the rebar tracing direction.
- Controlling the separation between rebars.

Once the rebar layout tracing is complete, we filter and translate the control points of each polyline by a distance $h/2$ or $-h/2$ along the unit normals of the mesh, so that the geometry of the rebars lies in the middle of the layer where the principal tensile stress occurs. We rebuild the polylines after shifting their control points.

Seeding Automation: Every rebar polyline starts from a seed point. The location of a seed point can be arbitrary, but the choice may lead to inadequate layouts. To procure an evenly distributed layout, we derive all the possible seed points at a given distance from an existing polyline before moving on to another (Jobard and Lefer 1997). Figure 10.1 depicts this seeding rule. Every polyline is sampled equi-distantly by length u_l and each of the resultant points is offset on the mesh by a rebar separation distance d_{su} or d_{sv} (hereafter d_s for notation simplicity) to the right and to the left of the polyline.

Priority Queue: It is desirable to enhance the structural integrity of a rebar layout by populating first the mesh regions requiring more reinforcement. We utilize a priority queue to this end. Every time a new seed point is created, we insert the point in the queue with a priority equal to the area of rebar a_{su} or a_{sv} needed at its current location on the mesh. The queue then schedules the release of new seed points, releasing points first in areas of the structure with the highest rebar demand. The priority queue stores and releases seed points until it is empty. Then, the tracing of rebar polylines stops.

Polyline Tracing: A polyline representing one rebar is traced by placing points on the mesh over a finite number of steps. At every step, the polyline grows by translating the seed point on the mesh by an extension distance d_l, in the direction of the average of the k PSDs closest to the point using first-order Euler integration (Figure 10.2). Small values of d_l are ideal to generate rebars that closely follow the PSDs (Halpern et al. 2013). After translation, the point is projected back to the mesh. The rebar tracing continues iteratively until the polyline hits the boundaries of the mesh, or until any of the distance control thresholds are met.

Distance Control: To ensure an evenly distributed layout, we aim to have no pair of rebars closer to each other than any of the proximity thresholds p_1, p_2 and p_3. These thresholds are computed based on the rebar separation distances d_s:

$$p_1 = d_s\, s_1 \qquad p_2 = d_s\, s_2 \qquad p_3 = d_s\, s_3 \qquad (7)$$
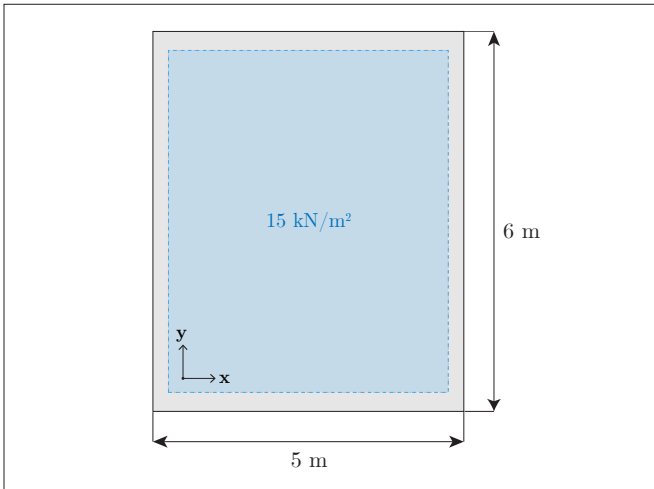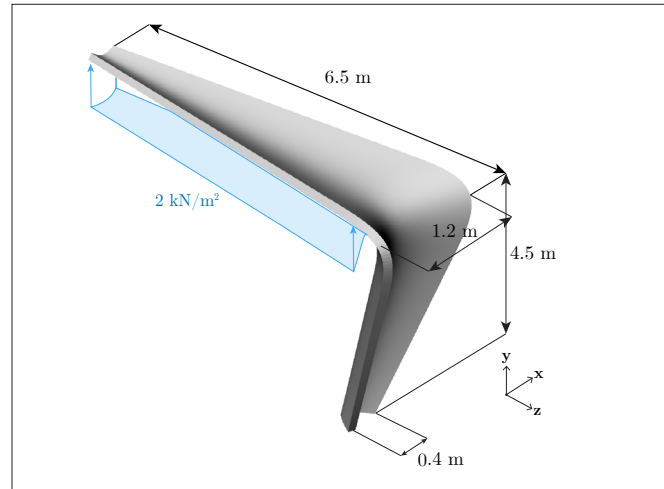
11 RC surfaces: geometry and applied loads:

  11.1 Flat slab

  11.2 Folded shell

Proximity factor s_1 defines the allowable distance of one rebar to the others at the first tracing iteration. Values that range between 0.8 and 1 are adequate. Factor s_2 controls the separation among rebars at any other stage of the tracing algorithm. Values under 0.5 lead to predominantly long rebars (Jobard and Lefer 1997). In zones where circumferential stresses exist, rebars tend to indefinitely turn around themselves. Therefore, the proximity factor s_3 is introduced to check the proximity of a polyline to itself. Values between 1 and 3 are suitable.

At every iteration, we calculate these proximity thresholds based on the distance between the moving seed point of a traced rebar and the control points of all traced rebar polylines and itself (Figure 10.3). If any of the thresholds is exceeded, then the tracing of a polyline stops and the tracing process moves on to the next seed in the queue.

STRUCTURAL APPLICATIONS

We showcase the effectiveness of our method by generating rebar layouts for two RC surfaces: a rectangular slab plate and a folded cantilevering shell.

The first structure reproduces a design from Lourenço and Figueiras (1993). The slab is fixed along its perimeter with pinned supports, and subjected to an out-of-plane, uniformly distributed load of 15 kN/m². The slab has a constant thickness of $t = 15$ cm, and is shown in Figure 11.1.

The folded shell in Figure 11.2 is a 3D structure subjected to an uplifting uniform load of 2 kN/m². The shell is restrained with pinned supports at the base, and has a constant thickness of $t = 17$ cm. For both structures, the yield strength of reinforcement steel is $f_y = 500$ MPa. We set the distance between top and bottom layers to $h = 0.9t$.

In these experiments, we generate a rebar layout aligned with the PSDs for each structure, and benchmark it in terms of the rebar demand against a single orthogonal grid, a typical layout in construction practice. We set the reference axes $\mathbf{u}$ and $\mathbf{v}$ as the Cartesian vectors $\mathbf{x}$ and $\mathbf{y}$ for the baseline orthogonal layouts, respectively; and as $\boldsymbol{\sigma}_1$, $\boldsymbol{\sigma}_2$ for the layouts that follow the PSDs.

Figures 12 and 13 show the rebar distributions in the slab calculated via Equation 5. The slab requires most rebar at the bottom layer as it experiences positive bending moments that exert tensile stresses on the soffit. There, rebar smears from 0 to 5.1 cm²/m on directions $\mathbf{x}$ and $\boldsymbol{\sigma}_1$; and from 0 to 4.1 cm²/m along $\mathbf{y}$ and $\boldsymbol{\sigma}_2$. In the bottom layer, rebar has a similar cross-like spread along $\mathbf{x}$ and $\boldsymbol{\sigma}_1$ (Figures 12.1 and 13.1), but it differs between $\mathbf{y}$ and $\boldsymbol{\sigma}_2$: in the latter case, rebar radiates elliptically from the midspan and vanishes towards the four corners of the slab (Figures 12.3 and 13.3). In the top layer, we highlight that the alignment with the optimal force flow suppresses the need for rebar along $\boldsymbol{\sigma}_1$ (Figure 13.2). In contrast, the orthogonal layout requires up to 3.6 cm²/m of rebar along $\mathbf{x}$ in the top layer (Figure 12.2).

The distribution of rebar along $\mathbf{y}$ and $\boldsymbol{\sigma}_2$ is comparable for the cantilevering shell, requiring a maximum of 16.7 cm²/m at the base of the structure for both alignment types (Figures 14.2 and 14.4). Along $\mathbf{x}$ and $\boldsymbol{\sigma}_1$, however, the spread of rebar demand varies from one alignment to the other, particularly where the surface folds and transitions from the vertical to a horizontal cantilever (Figures 14.1

12.1   12.2   12.3   12.4

13.1   13.2   13.3   13.4
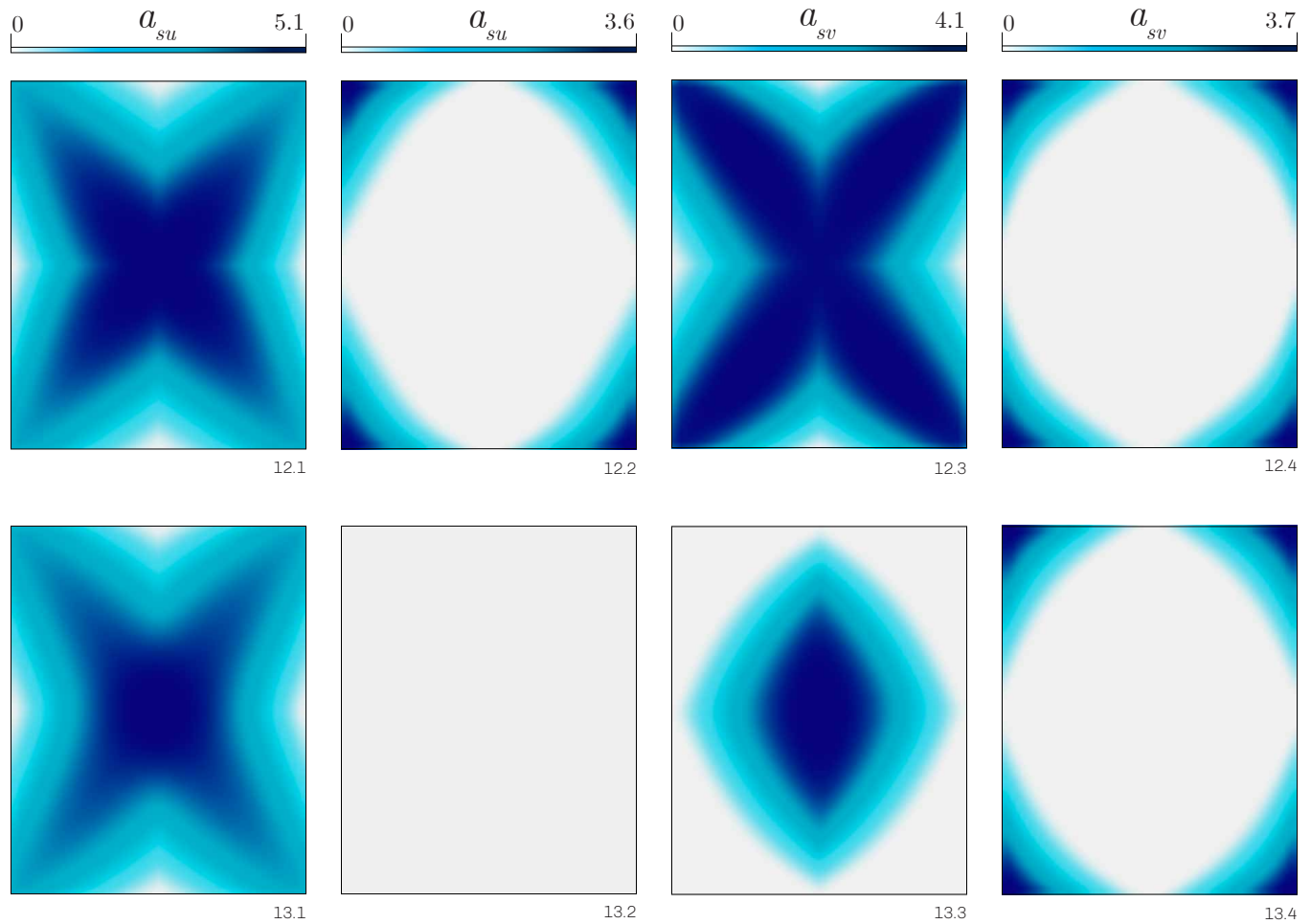
and 14.3). The maximum rebar demand along $\mathbf{x}$ and $\boldsymbol{\sigma}_1$ is 4.1 cm²/m, but the area with high reinforcement demand occupies a larger portion of the structure in the baseline alignment, thus indicating the need for more rebar along $\mathbf{x}$ than along $\boldsymbol{\sigma}_1$.

Figure 15 summarizes the total area of rebar steel calculated with Equation 5 required to carry tensile stresses for both RC surfaces, detailing the contribution that every layer has to the total steel demand. The reported areas are normalized, with respect to the orthogonal layout areas, to show changes in rebar demand relative to the baseline configuration. Aligning rebars with the PSDs reduces the rebar steel required to resist tensile stresses. The layouts that follow the PSDs require only 68% and 90% of the total area of steel per unit width a_s^{total} needed by the reference layout: 32% and 10% less than the baseline, respectively.

Aligning rebars with the PSDs saves more steel in one direction than in the other. In the slab, 24% of the steel savings relative to the baseline stem from aligning the rebar at the bottom layer with $\boldsymbol{\sigma}_2$. In contrast, there is only a 1% difference between $\mathbf{x}$ and $\boldsymbol{\sigma}_1$ in the same layer. In the

12   Rebar distribution per slab layer with the baseline alignment ($\mathbf{x}$, $\mathbf{y}$):

    12.1 Direction $\mathbf{x}$, bottom layer

    12.2 Direction $\mathbf{x}$, top layer

    12.3 Direction $\mathbf{y}$, bottom layer

    12.4 Direction $\mathbf{y}$, top layer

13   Rebar distribution per slab layer with the PSDs alignment ($\boldsymbol{\sigma}_1$, $\boldsymbol{\sigma}_2$):

    13.1 Direction $\boldsymbol{\sigma}_1$, bottom layer

    13.2 Direction $\boldsymbol{\sigma}_1$, top layer

    13.3 Direction $\boldsymbol{\sigma}_2$, bottom layer

    13.4 Direction $\boldsymbol{\sigma}_2$, top layer

folded shell, there is an 8% difference in rebar area demand between the $\boldsymbol{\sigma}_1$ and $\mathbf{x}$ alignments in favor of the former. Moreover, all the rebars are hosted in the bottom layer of the shell (i.e., rebar is not needed in the top layer) due to the bending moment caused by the applied uplifting load.

Besides the difference in the magnitude of the applied loads, a plausible reason why rebar reductions are more prominent in the slab than in the shell is that the former is a flat structure where out-of-plane moments are high and must
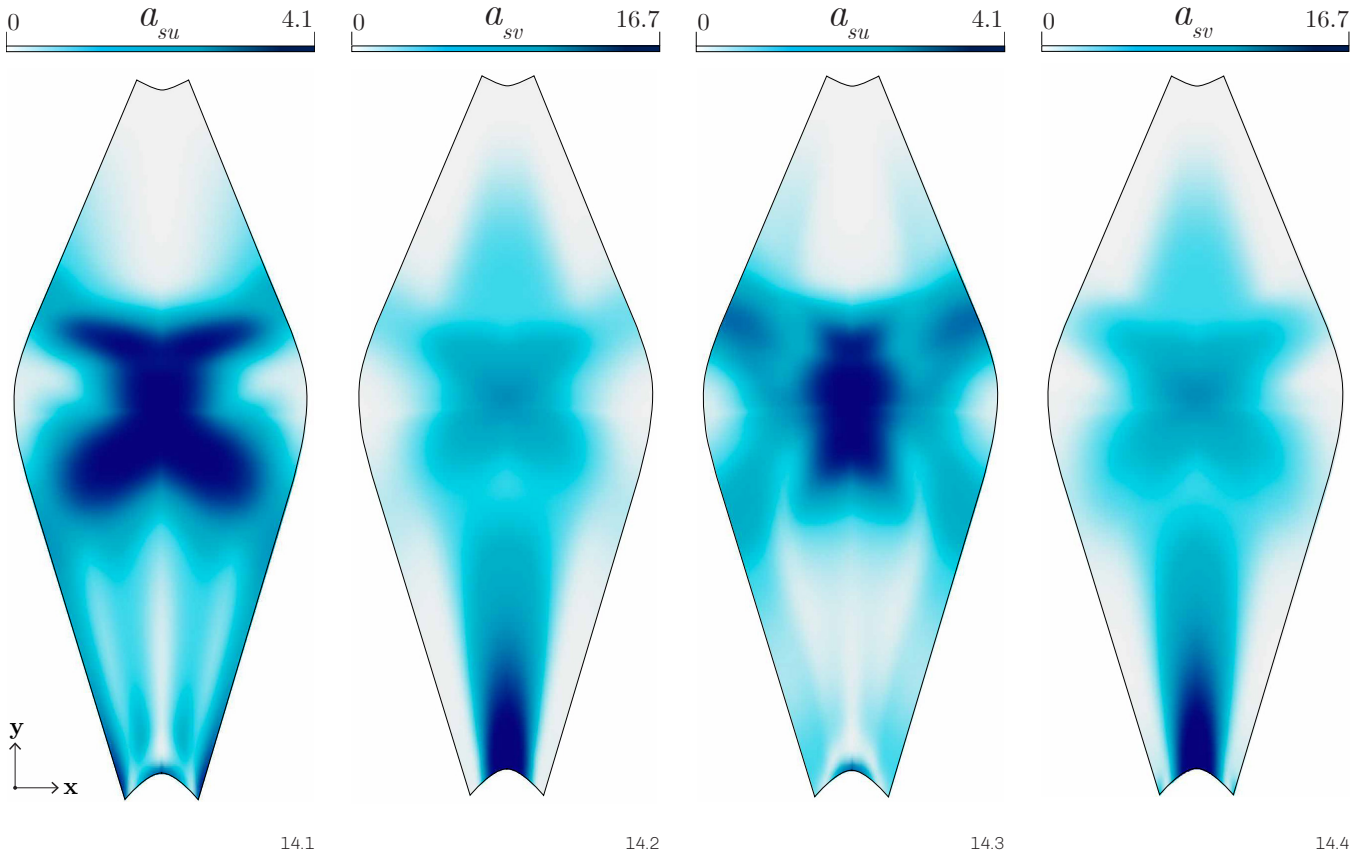
14 Rebar distribution in the folded shell:

    14.1 Direction **x**

    14.2 Direction **y**

    14.3 Direction $\boldsymbol{\sigma}_1$

    14.4 Direction $\boldsymbol{\sigma}_2$

15 Normalized reinforcement areas for

    the baseline (**x**, **y**) and the PSDs ($\boldsymbol{\sigma}_1$, $\boldsymbol{\sigma}_2$).

| Structure	Rebar orientation	a_{su}^{b}	a_{su}^{t}	a_{sv}^{b}	a_{sv}^{t}	a_{s}^{total}
Flat slab	Baseline (**x**, **y**)	0.46	0.07	0.40	0.07	1.00
	Stress-aligned ($\boldsymbol{\sigma}_1$, $\boldsymbol{\sigma}_2$)	0.45	0.00	0.16	0.07	**0.68**
Folded shell	Baseline (**x**, **y**)	0.31	0.00	0.69	0.00	1.00
	Stress-aligned ($\boldsymbol{\sigma}_1$, $\boldsymbol{\sigma}_2$)	0.23	0.00	0.67	0.00	**0.90**

15

be resisted predominantly by rebar steel; whereas, in the latter, the curved folded shape activates the in-plane axial strength of the shell, thus decreasing the reliance on rebar. This suggests that a PSDs-aligned layout can yield higher material savings on flat surfaces than on folded structures whose main load-bearing mechanism is membrane action.
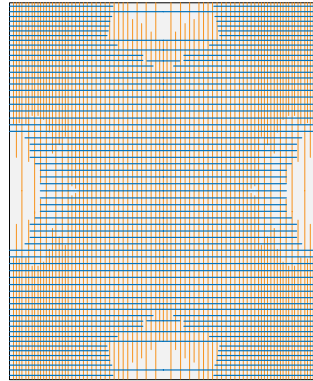
Next, we generate rebar layouts for the baseline single-grid case and the PSDs alignment case on both structures. These layouts correspond to the rebar area distributions presented in Figures 12, 13, and 14. In the baseline case, we only present the layout in the bottom layer of the slab. For the slab layouts, we select two different groups of diameters to study the effect that this parameter has on the spacing between rebars: a) 1 cm and 0.8 cm, and b) 0.8 cm and 0.6 cm. Each group of diameters assigns constant

rebar values $\boldsymbol{\phi}_u$ and $\boldsymbol{\phi}_v$ to the directions corresponding to the reference axes **u** and **v**, respectively. We run the tracing algorithm with $d_l = 2$ cm; $u_l = 10$ cm; $k = 3$; $s_1 = 0.9$; $s_2 = 0.5$; and $s_3 = 2$. For the shell, we assign rebars of constant diameter $\boldsymbol{\phi}_u = \boldsymbol{\phi}_v = 0.8$ cm on both directions and keep the same tracing parameters as for the slab, except for s_2, which we lower from 0.5 to 0.1.

In both structures and both alignment types, the layouts computed with our method adaptively spaced out, guided by the distances we calculate with Equations 5 and 6. Our method traces and densifies rebar to maintain the features of the required steel distribution to bear tensile stress, while depositing rebar only where it is structurally required (Figures 16, 17, and 18). Using larger diameters results in fewer rebars per layout, as the spacing between
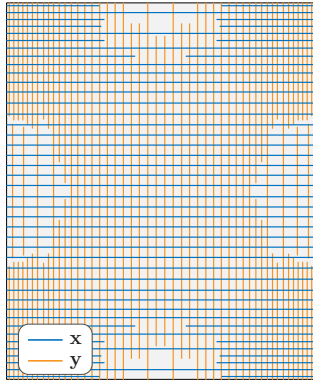
16 Rebar layouts for the slab with the baseline alignment ($\mathbf{x}$, $\mathbf{y}$):

    16.1 Diameters ϕ_u = 1 cm, ϕ_v = 0.8 cm

    16.2 Diameters ϕ_u = 0.8 cm, ϕ_v = 0.6 cm

17 Rebar layouts for the slab with the PSDs alignment ($\boldsymbol{\sigma}_1$, $\boldsymbol{\sigma}_2$):
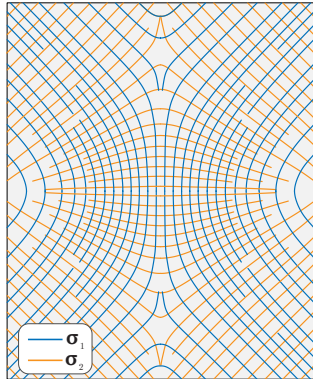
    17.1 Diameters ϕ_u = 1 cm, ϕ_v = 0.8 cm

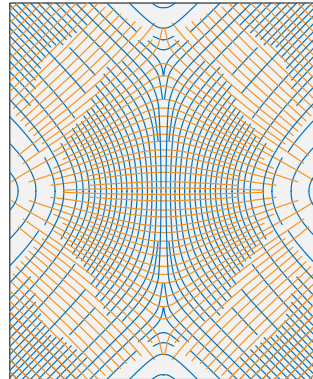   17.2 Diameters ϕ_u = 0.8 cm, ϕ_v = 0.6 cm

18 Rebar layouts for the folded shell, $\phi_u = \phi_v$ = 0.8 cm:

    18.1 Baseline alignment ($\mathbf{x}$, $\mathbf{y}$)

    18.2 PSDs alignment ($\boldsymbol{\sigma}_1$, $\boldsymbol{\sigma}_2$)

expands quadratically if the input rebar diameter increases (Equation 6). Conversely, using smaller diameters results in layouts with more rebars in order to provide the required tensile capacity to the RC structures.
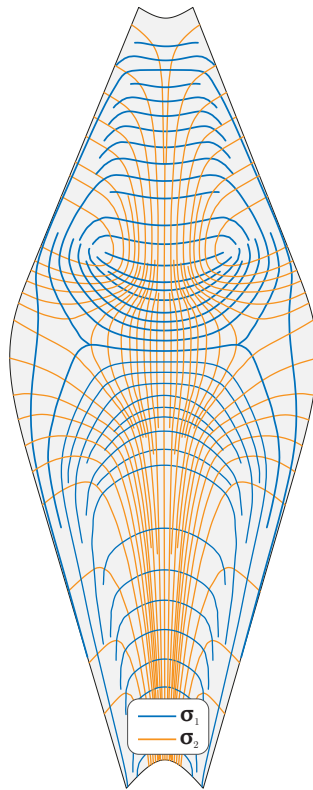
CONCLUSION

This paper presented a method to design rebar layouts aligned with the PSDs on RC architectural surfaces subject to a load case. By integrating a sandwich model for RC design, a priority queue-based seed generator and a distance-constrained tracing algorithm, our approach produced rebar layouts that effectively grade reinforcement steel based on the tensile stresses in an RC surface. This method thus overcomes some of the limitations of other current approaches and can support the design exploration of layouts in the conceptual design stage.

Through two illustrative examples, we demonstrated the efficacy of aligning rebars with the PSDs. Our method resulted in a reduction of rebar area of 10% and 32%, compared to the single orthogonal grid layout employed in traditional construction. Most of the savings in rebar steel stemmed from aligning structural material with one of the two PSDs. This reduction in rebar consumption not only enhances material efficiency but also has the potential to decrease the embodied carbon footprint of RC structures.

The proposed distance-constrained rebar tracing approach is a greedy algorithm that operates based on local heuristic rules. Consequently, one limitation of our method is that it does not guarantee a globally optimal solution. Nevertheless, our aim is not to find a global solution, which might be computationally expensive or intractable for general structures. Instead, the goal of our method is to facilitate the exploration of different locally optimal rebar layouts. The convergence rate to a local optimum is, however, contingent on the selection of an appropriate input mesh resolution and parameter values, as well as on the presence of singularities among the PSDs.

16.1

16.2

17.1

17.2
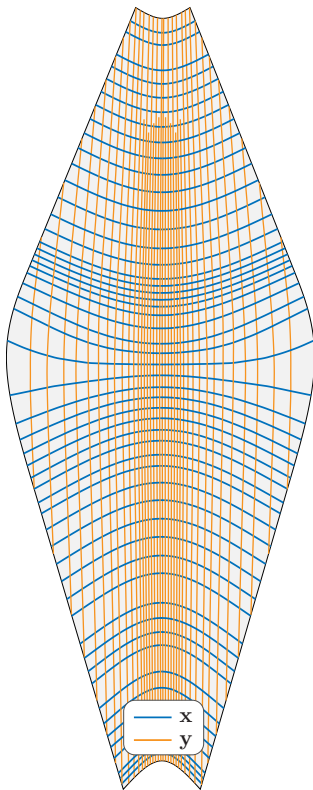
18.1

18.2

Looking ahead, we plan to incorporate higher-order integration methods to make the convergence rate of our tracing algorithm more robust to variations in the inputs. Another crucial aspect to consider is the inclusion of fabrication constraints during the tracing of the rebar polylines to generate layouts that are not only structurally informed and evenly distributed, but also increasingly suitable for construction using both analog and digital fabrication tools. While our focus has been on placing rebar steel along an ideal flow of forces, our framework can be extended to trace efficient reinforcement distributions for other filament types, such as carbon fibers or natural fibers, on different architectural surfaces.

In conclusion, our research advances the development of new digital methods to design rebar layouts, opening up opportunities in digital reinforcement research for improved structural efficiency, reduced material consumption, and enhanced sustainability.

ACKNOWLEDGEMENTS

REFERENCES

Addis, William. 2015. *Building: 3000 Years of Design Engineering and Construction*. London: Phaidon Press, Inc.

Andrew, Robbie M. 2019. "Global CO2 Emissions from Cement Production, 1928–2018." *Earth System Science Data* 11 (4): 1675–1710. https://doi.org/10.5194/essd-11-1675-2019.

Anton, Ana, Patrick Bedarf, Angela Yoo, Benjamin Dillenburger, Lex Reiter, Timothy Wangler, and Robert J. Flatt. 2020. "Concrete Choreography: Prefabrication of 3D-Printed Columns." https://doi.org/10.3929/ETHZ-B-000408884.

Asprone, Domenico, Costantino Menna, Freek P. Bos, Theo A.M. Salet, Jaime Mata-Falcón, and Walter Kaufmann. 2018. "Rethinking Reinforcement for Digital Fabrication with Concrete." *Cement and Concrete Research* 112: 111–21. https://doi.org/10.1016/j.cemconres.2018.05.020.

Bhooshan, Shajay, Vishu Bhooshan, Alessandro Dell'Endice, Jianfei Chu, Philip Singer, Johannes Megens, Tom Van Mele, and Philippe Block. 2022. "The Striatus Bridge: Computational Design and Robotic Fabrication of an Unreinforced, 3D-Concrete-Printed, Masonry Arch Bridge." *Architecture, Structures and Construction* 2 (4): 521–43. https://doi.org/10.1007/s44150-022-00051-y.

Blaauwendraad, Johan. 2010. *Plates and FEM: Surprises and Pitfalls*. Vol. 171. Solid Mechanics and Its Applications. Dordrecht: Springer Netherlands. https://doi.org/10.1007/978-90-481-3596-7.

European Committee for Standardization (ECS). 2005. "Eurocode 2. Design of Concrete Structures - Part 2: Concrete Bridges- Design and Detailing Rules." European Standard. Brussels: BSI British Standards. https://doi.org/10.3403/30096437.

Gantner, Stefan, Tom-Niklas Rothe, Christian Hühne, and Norman Hack. 2022. "Reinforcement Strategies for Additive Manufacturing in Construction Based on Dynamic Fibre Winding: Concepts and Initial Case Studies." Open Conference Proceedings 1: 45–59. https://doi.org/10.52825/ocp.v1i.78.

Hack, Norman, and Willi Viktor Lauer. 2014. "Mesh-Mould: Robotically Fabricated Spatial Meshes as Reinforced Concrete Formwork." Architectural Design 84 (3): 44–53. https://doi.org/10.1002/ad.1753.

Halpern, Allison B., David P. Billington, and Sigrid Adriaenssens. 2013. "The Ribbed Floor Slab Systems of Pier Luigi Nervi." *Journal of the International Association for Shell and Spatial Structures* 54 (2–3): 127–36.

Hecker, Hans-Dieter, and Sigrid Hecker. 2009. *Entwürfe Und Bauten*. Freiburg im Breisgau: Herder.

Hibbeler, Russell C. 2017. *Mechanics of Materials*. Tenth edition. Boston: Pearson.

International Federation for Structural Concrete (IFSC). 2008. Practitioners' Guide to Finite Element Modelling of Reinforced Concrete Structures: State-of-Art Report. 1. Bulletin / CEB-Fib State-of-Art Report 45. Lausanne: International Federation for Structural Concrete (fib).

Jipa, Andrei, Cristián Calvo Barentin, Gearóid Lydon, Matthias Rippmann, Georgia Chousou, Matteo Lomaglio, Arno Schlüter, Philippe Block, and Benjamin Dillenburger. 2019. "3D-Printed Formwork for Integrated Funicular Concrete Slabs." In Proceedings of IASS Annual Symposia, 2019:1–8. Barcelona, Spain. https://www.ingentaconnect.com/content/iass/piass/2019/00002019/00000006/art00006

Jobard, Bruno, and Wilfrid Lefer. 1997. "Creating Evenly-Spaced Streamlines of Arbitrary Density." In Visualization in Scientific Computing '97, edited by Wilfrid Lefer and Michel Grave, 43–55. Eurographics. Vienna: Springer. https://doi.org/10.1007/978-3-7091-6876-9_5.

Lloret, Ena, Amir R. Shahab, Mettler Linus, Robert J. Flatt, Fabio Gramazio, Matthias Kohler, and Silke Langenberg. 2015. "Complex Concrete Structures." *Computer-Aided Design* 60: 40–49. https://doi.org/10.1016/j.cad.2014.02.011.

Lourenço, Paulo B., and Joaquim A. Figueiras. 1993. "Automatic Design of Reinforcement in Concrete Plates and Shells." *Engineering Computations* 10 (6): 519–41. https://doi.org/10.1108/eb023923.

Lourenço, Paulo B., and Joaquim A. Figueiras. 1995. "Solution for the Design of Reinforced Concrete Plates and Shells." *Journal of Structural Engineering* 121 (5): 815–23. https://doi.org/10.1061/(ASCE)0733-9445(1995)121:5(815).

Lowke, Dirk, Aileen Vandenberg, Alexandre Pierre, Amaury Thomas, Harald Kloft, and Norman Hack. 2021. "Injection 3D Concrete Printing in a Carrier Liquid - Underlying Physics and Applications to Lightweight Space Frame Structures." *Cement and Concrete Composites* 124: 104169. https://doi.org/10.1016/j.cemconcomp.2021.104169.

Ma, Zhao, Alexander Walzer, Christian Schumacher, Romana Rust, Fabio Gramazio, Matthias Kohler, and Moritz Bächer. 2020. "Designing Robotically-Constructed Metal Frame Structures." *Computer Graphics Forum* 39 (2): 411–22. https://doi.org/10.1111/cgf.13940.

Mebarki, Abdelkrim, Pierre Alliez, and Olivier Devillers. 2005. "Farthest Point Seeding for Efficient Placement of Streamlines." In IEEE Visualization 2005 - (VIS'05), 61–61. Minneapolis, MN, USA: IEEE. https://doi.org/10.1109/VIS.2005.39.

Michalatos, Panagiotis, and Sawako Kaijima. 2014. "Eigenshells: Structural Patterns on Modal Forms." In Shell Structures for Architecture: Form Finding and Optimization, 1st ed. London: Routledge. https://doi.org/10.4324/9781315849270.

Michell, Anthony George Maldon. 1904. "LVIII. The Limits of Economy of Material in Frame-Structures." *The London, Edinburgh, and Dublin Philosophical Magazine and Journal of Science* 8 (47): 589–97. https://doi.org/10.1080/14786440409463229.

Miller, Dane, Jeung-Hwan Doh, and Mitchell Mulvey. 2015. "Concrete Slab Comparison and Embodied Energy Optimisation for Alternate Design and Construction Techniques." *Construction and Building Materials* 80 (April): 329–38. https://doi.org/10.1016/j.conbuildmat.2015.01.071.

Mirjan, Ammar, Jaime Mata-Falcón, Carsten Rieger, Janin Herkrath, Walter Kaufmann, Fabio Gramazio, and Matthias Kohler. 2022. "Mesh Mould Prefabrication." In Third RILEM International Conference on Concrete and Digital Fabrication, edited by Richard Buswell, Ana Blanco, Sergio Cavalaro, and Peter Kinnell, 31–36. https://doi.org/10.1007/978-3-031-06116-5_5.

Nervi, Pier Luigi, Carlo Maria Olmo, Cristiana Chiorino, Christophe Pourtois, Marcelle Rabinowicz, and Elisabetta Margiotta Nervi. 2010. *Pier Luigi Nervi: Architecture as Challenge*. Cinisello Balsamo, Milano: Silvana.

Oval, Robin, Eduardo Costa, Diana Thomas-Mcewen, Saverio Spadea, John Orr, and Paul Shepherd. 2020. "Automated Framework for the Optimisation of Spatial Layouts for Concrete Structures Reinforced with Robotic Filament Winding." In . Kitakyushu, Japan. https://doi.org/10.22260/ISARC2020/0214.

Oval, Robin, Mishael Nuh, Eduardo Costa, Omar Abo Madyan, John Orr, and Paul Shepherd. 2023. "A Prototype Low-Carbon Segmented Concrete Shell Building Floor System." *Structures* 49 (March): 124–38. https://doi.org/10.1016/j.istruc.2023.01.063.

Pellis, Davide, and Helmut Pottmann. 2018. "Aligning Principal Stress and Curvature Directions." In Advances in Architectural Geometry, edited by Lars Hesselgren, Axel Kilian, Samar Malek, Karl-Gunnar Olsson, Olga Sorkine-Hornung, and Chris Williams, 34–53. Klein Publishing Ltd.

Preisinger, Clemens, and Moritz Heimrath. 2014. "Karamba—A Toolkit for Parametric Structural Design." *Structural Engineering International* 24 (2): 217–21. https://doi.org/10.2749/101686614X13830790993483.

Tam, Kam-Ming Mark, and Caitlin T. Mueller. 2015. "Stress Line Generation for Structurally Performative Architectural Design." In Proceedings of the 35th Annual Conference of the Association for Computer Aided Design in Architecture (ACADIA), 95-109. Cincinnati: USA. https://doi.org/10.52842/conf.acadia.2015.095

Van Mele, Tom, Gonzalo Casas, Romana Rust, and Mathias Bernhard. 2017. "COMPAS: A Framework for Computational Research in Architecture and Structures." https://doi.org/10.5281/zenodo.2594510.

Wang, Tao, Daniel B. Müller, and T. E. Graedel. 2007. "Forging the Anthropogenic Iron Cycle." *Environmental Science & Technology* 41 (14): 5120–29. https://doi.org/10.1021/es062761t.

Wangler, Timothy, Nicolas Roussel, Freek P. Bos, Theo A. M. Salet, and Robert J. Flatt. 2019. "Digital Concrete: A Review." *Cement and Concrete Research* 123: 105780. https://doi.org/10.1016/j.cemconres.2019.105780.

IMAGE CREDITS

_____

Rafael Pastrana is a Ph.D. candidate at the Princeton University School of Architecture. He develops computational methods and tools to solve complex structural design problems. Rafael holds a master's degree in architecture and digital fabrication from ETH Zurich. His professional experience, at the intersection of structural and software engineering, includes working at Bollinger + Grohmann, the Block Research Group, and Robert McNeel and Associates.

_____

Zhao Ma is a multidisciplinary researcher and educator with a background in design, engineering, and computer science. He is a lecturer and senior researcher at ETH Zurich, where he teaches computational methods for design education, and conducts research on computing applications for living systems, geometry processing, and robotic fabrication. Zhao received two master's degrees from MIT in 2017, and a doctoral degree from ETH Zurich in 2021, conducting cross-disciplinary research across the fields of architecture and computer graphics. His doctoral work, Stylized Robotic Sculpting, developed a novel design and fabrication system for carving clay sculptures utilizing robots.